Supporting Information for: "Excited State Dynamics during Primary C–I Homolysis in Acetyl Iodide revealed by Ultrafast Core-Level Spectroscopy"

Jan Troß,[a,] Kevin Carter-Fenk,[b,*]Neil C. Cole-Filipiak,[a] Paul Schrader,[a] Mi'Kayla Word,[a] Laura M. McCaslin,[a] Martin Head-Gordon,[b,c,†]and Krupa Ramasesha[a,‡]

[a] *Combustion Research Facility, Sandia National Laboratories, Livermore, CA 94551, USA*

[b] *Department of Chemistry, University of California, Berkeley, CA 94720, USA*

[c] *Chemical Sciences Division, Lawrence Berkeley National Laboratory, Berkeley, CA 94720, USA*

April 12, 2023

*carter-fenk@berkeley.edu

†mhg@cchem.berkeley.edu

‡kramase@sandia.gov

S1 Valence electronic structure and UV/Vis absorption spectra of acetyl halides

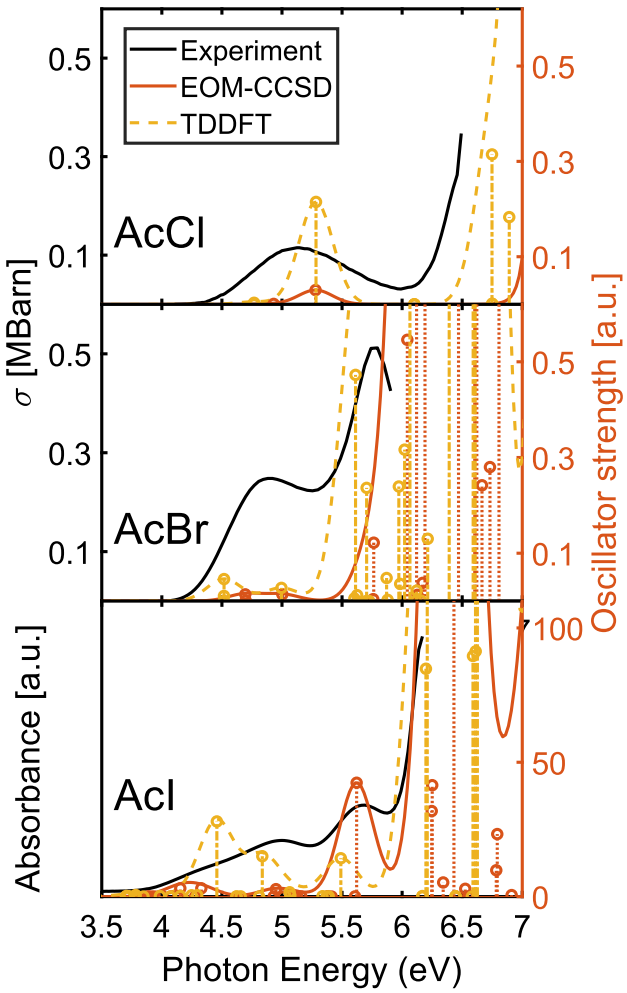

Figure S1: Additional comparison between experimental and calculated UV/visible absorption spectra of gas-phase acetyl halides, based on TDDFT and EOM-CCSD. Absorption cross sections of gas-phase AcCl (top panel), AcBr (middle panel), and absorption spectrum of AcI at 32 Torr static pressure between 3.5 and 7 eV (bottom panel). Experimental data for AcCl and AcBr are adapted with permission from Refs. 1 and 2, respectively.

In addition to EOM-CCSD calculations of the UV/visible absorption spectra of acetyl halides, herein, we also report TDDFT calculations of these spectra in Fig. S1, as we use TDDFT for the *ai*MD simulations. We computed TDDFT spectra using ORCA v5.0.3[3] at the ωB97X-D3[4] level using the aug-cc-pVTZ-DK basis set for C, H, O, Cl, and Br atoms with the aug-cc-pwCVTZ-DK3 basis for I.[5–7] All TDDFT calculations employ a fine `DefGrid3`[8] quadrature and account for scalar relativistic effects through the second-order Douglas-Kroll-Hess Hamiltonian[9–11] along with spin-orbit couplings via the Breit-Pauli Hamiltonian.[12]

S2 XUV absorption spectra of Acetyl Iodide

Whereas the absorption spectrum of acetyl iodide in Figure S2 shows only four sharp absorption features, the differential measurement (using a mechanical shutter to more rapidly acquire reference spectra) is able to detect bleach features associated with AcI at 61.2 and 62.9 eV, as seen in Figure S3. A broad negative differential absorption between 55 and 65 eV is overlapped with sharp induced absorption features at 55.5 and 57.5 eV, which are associated with free iodine.

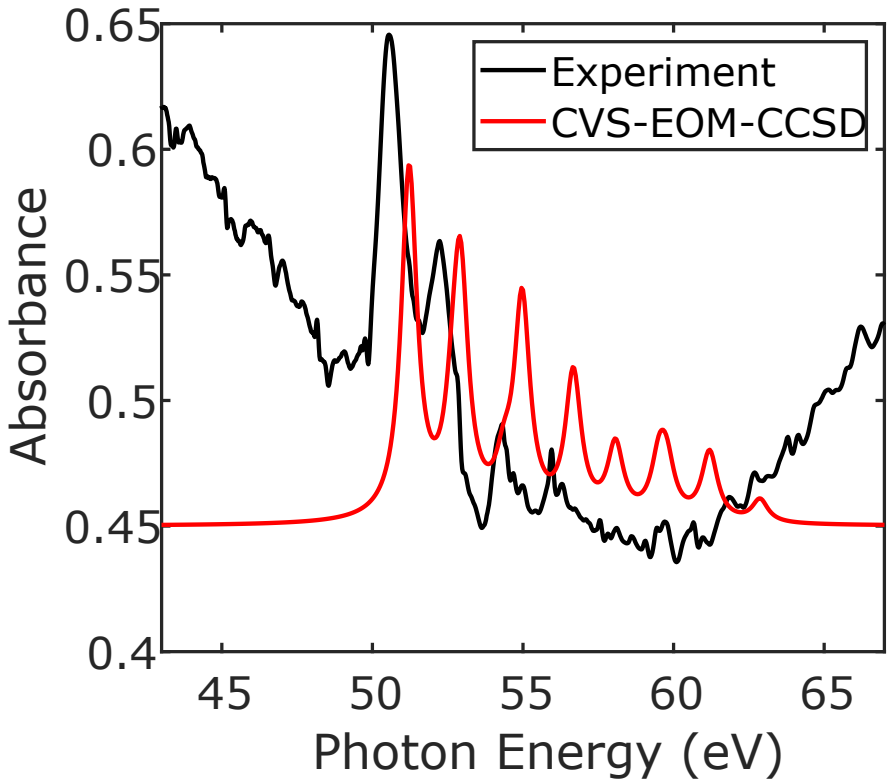

Figure S2: Raw experimental XUV absorption spectrum of acetyl iodide in comparison to CVS-EOM-CCSD calculations. The measured spectrum shows a broad, 0.45-0.65 OD absorption over the entire detector range.

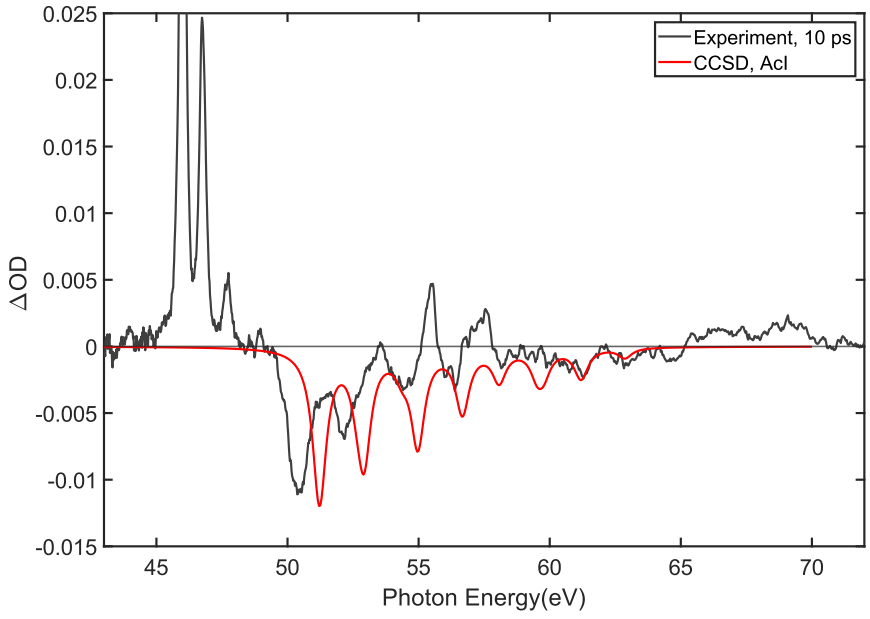

Figure S3: Differential absorption spectrum of acetyl iodide at a time delay of 10 ps in comparison to CVS-EOM-CCSD predicted spectrum. A negative change in OD is observed up to 65 eV and dips at 61.2 and 62.9 eV match between experiment and calculations

S3 Additional false color map

In Fig. S4, we provide the reader with an alternative color map figure for the experimental transient XUV spectra. Additionally, data up to a delay of 1 ps is shown.

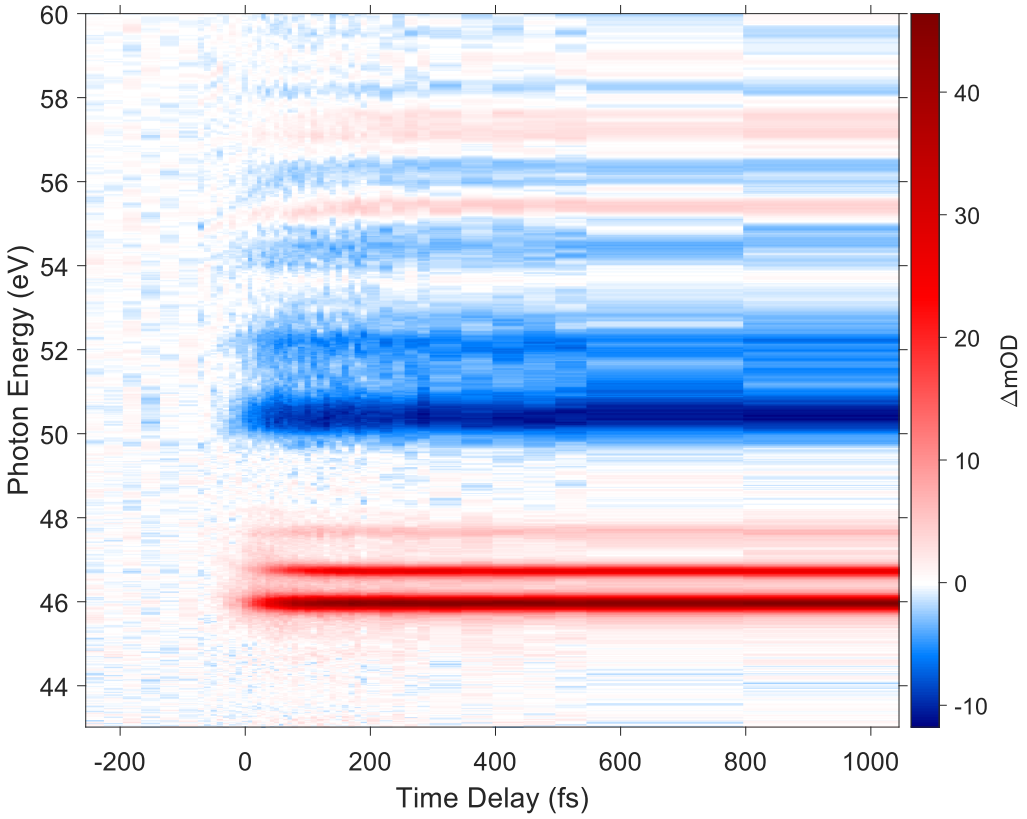

Figure S4: Alternative false color map of the transient XUV absorption spectra of 266-nm excited gas-phase acetyl iodide for time delays of -250 fs to 1 ps. Parallel pump and probe polarization was used for this data.

S4 Description of the fit function

The rise of the atomic iodine absorption and the acetyl iodide bleach features, which trend towards global maximum absolute intensities as a function of time, can be described by a cumulative distribution function with a rise time σ. When convolved with a Gaussian IRF, we get the following equation, which we use to fit these data:

$$S_{rise}(\Delta t) = S_0 + A(1 + erf((\Delta t - t_0 - t_{shift})/\sigma_{IRF}) - (exp(\sigma_{IRF}^2 - \\ - 4\sigma(\Delta t - t_0 - t_{shift}))/4\sigma^2))(1 - erf((\sigma_{IRF}^2 - \\ - 2\sigma(\Delta t - t_0 - t_{shift}))/(2\sigma_{IRF}\sigma)))) \quad \text{(S1)}$$

where S_0, A, t_{shift} and σ are fit parameters. S_0 is the signal before t_0, A is the amplitude of the signal at long time delays, $erf((\Delta t - t_0 - t_{shift})$ is the error function, and Δt the experimental delay between pump and probe. σ_{IRF} is the instrument response function, σ the extracted rise of the signal as reported in the main article, and t_{shift} the reported offset to the experimentally verified true time-zero of t_0.

The decay of the 47.1 eV feature to zero intensity as a function of time can be described by an exponential decay with a decay time σ. When convolved with a Gaussian IRF, the fit equation is given by

$$S_{decay}(\Delta t) = S_0 + A(exp((\sigma_{IRF}^2 - 4\sigma(\Delta t - t_0 - t_{shift}))/(4\sigma^2)) \\ (1 - erf((\sigma_{IRF}^2 - 2\sigma(\Delta t - t_0 - t_{shift}))/(2(\sigma_{IRF})\sigma)))) \quad \text{(S2)}$$

where S_0, A, t_{shift} and σ are again fit parameters, while here A describes the amplitude of the signal before it decays.

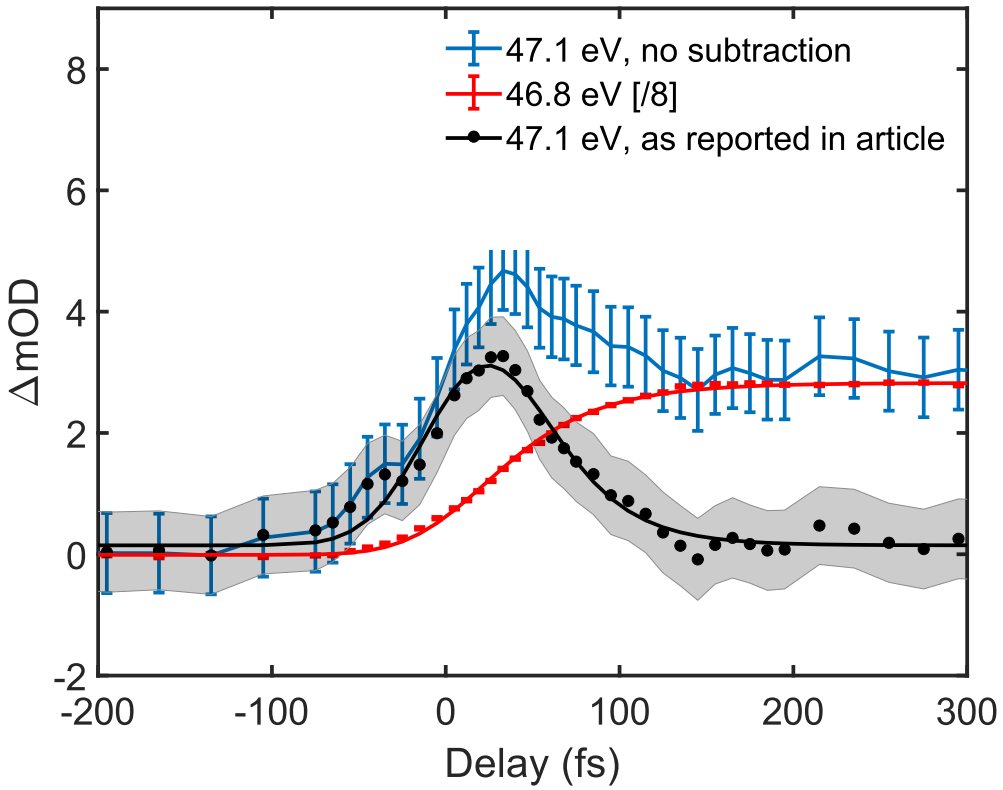

Figure S5: Integrated differential absorbance of the 47.1 eV feature, which is subtracted by a scaled CDF of the signal at 46.8 eV, resulting in the black curve (as reported in the main article).The black and red solid lines are fits to the experimental data.

S5 Experimental data for perpendicular relative pump and probe polarizations

The main text discussed the transient spectral features for the parallel pump and probe polarization geometry. Here, we describe the differences in our experimental results between the parallel and perpendicular polarization geometries.

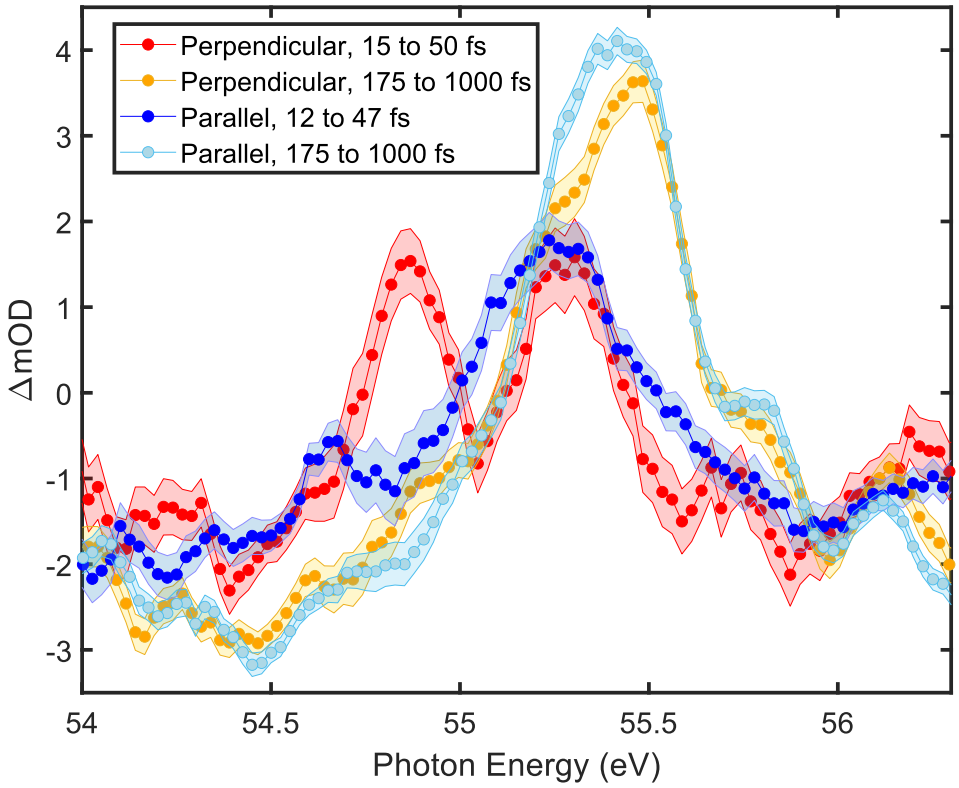

Figure S6: Differential absorbance between 54 and 57 eV for acetyl iodide integrated across time windows: 15 to 50 fs and 175 to 1000 fs. In the early time window, we observe two peaks at 54.9 and 55.3 eV for perpendicular polarization, whereas we only observe one peak at 55.3 eV for parallel polarization. In the later time window, we observe one peak at 55.5 eV for both polarizations.

Whereas the spectral features associated with the bleach of ground state AcI and the induced absorption of free I and I* are identical for the two polarization geometries for time delays longer than 300 fs, at short, sub-100 fs time delays, the differential absorption with perpendicular polarized pump and probe (p-polarized XUV and s-polarized UV) show subtle differences from the parallel polarization case. In the perpendicular polarization geometry, the absorption features between 43 and 48 eV exhibit a σ of 43 ± 5 fs and an offset of 30 ± 5 fs for I ($^2P_{3/2} \rightarrow {}^2D_{5/2}$) at 46.1 eV and I*($^2P_{1/2} \rightarrow {}^2D_{3/2}$) at 46.8 eV, which aligns with the findings for parallel polarization. However, a shift in center of mass for I*($^2P_{1/2} \rightarrow {}^2D_{3/2}$) from 46.9 to 46.8 eV in the vicinity of t_0 is seen for the perpendicular polarization case that was only 20 meV in the parallel polarization case. A more pronounced difference is observed for the spectral region of 54 to 57 eV. We compare early time spectra (integrated across 15 fs $< \Delta t <$ 50 fs) and late time spectra (integrated across 175 fs $< \Delta t <$ 1 ps) in the 54 to 57 eV range, as displayed in Figure S6. For both polarizations, there is a shift of the absorption maximum for the I ($4d \rightarrow 5p$) from 55.3 eV to 55.5 eV over the first 100 fs as described in the main manuscript, but for perpendicular polarization, there is a separate feature at 54.9 eV at early time delays. We see an overlapping bleach centered at 54.5 eV that influences the delay dependent differential absorption at 54.9 eV; in order to account for this, we subtract a scaled Gaussian cumulative distribution function from the delay dependent differential absorption and extract temporal widths and offsets. This fit of the temporal behavior of the 54.9 eV feature results in a width of 110 ± 20 fs FWHM and a maximum in time at 43 ± 10 fs with respect to t_0.

At present, we refrain from interpreting the experimental perpendicular data, as theoretical methods are currently not equipped and verified for predicting cross polarized spectra. This is because the tensor components of the polarization are not recovered in normal linear response theories. To do so, a sum-over-states evaluation of the polarizability could recover the tensor components but this technology is not implemented with the core-valence separation approximation employed in the present calculation.

S6 266 nm power dependence study

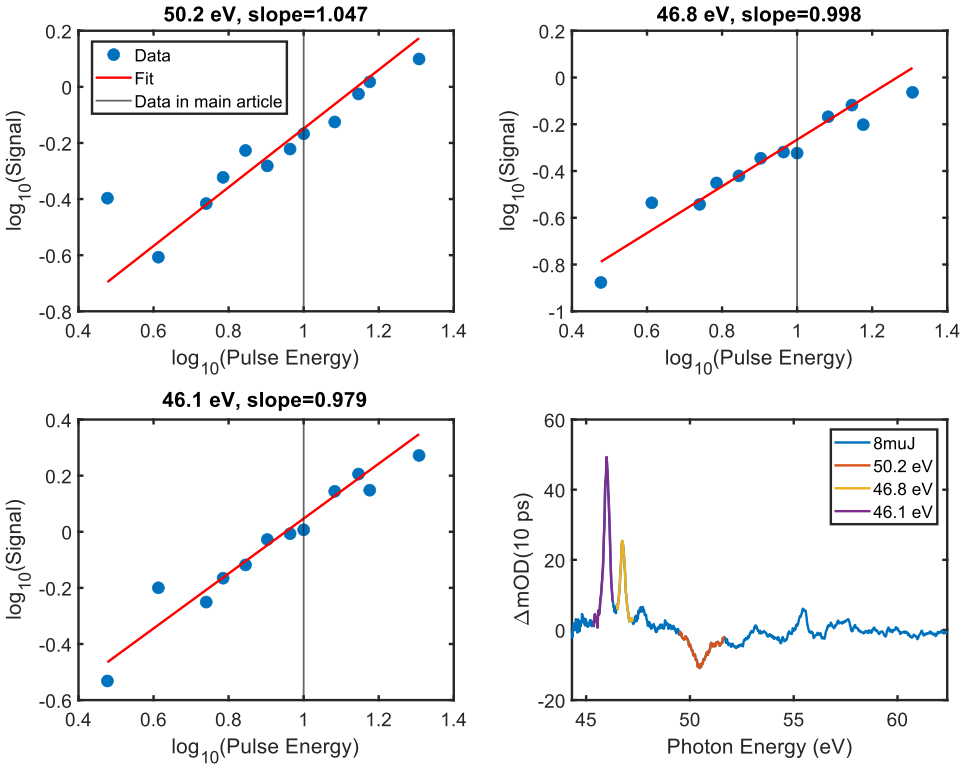

Figure S7: Dependence of transient signal at the indicated energy ranges on 266 nm pulse energy, showing nearly one-photon dependence. Vertical grey line indicates the chosen 266-nm pulse energy for acquiring the data presented in the main paper.

S7 Determination of the experimental time resolution

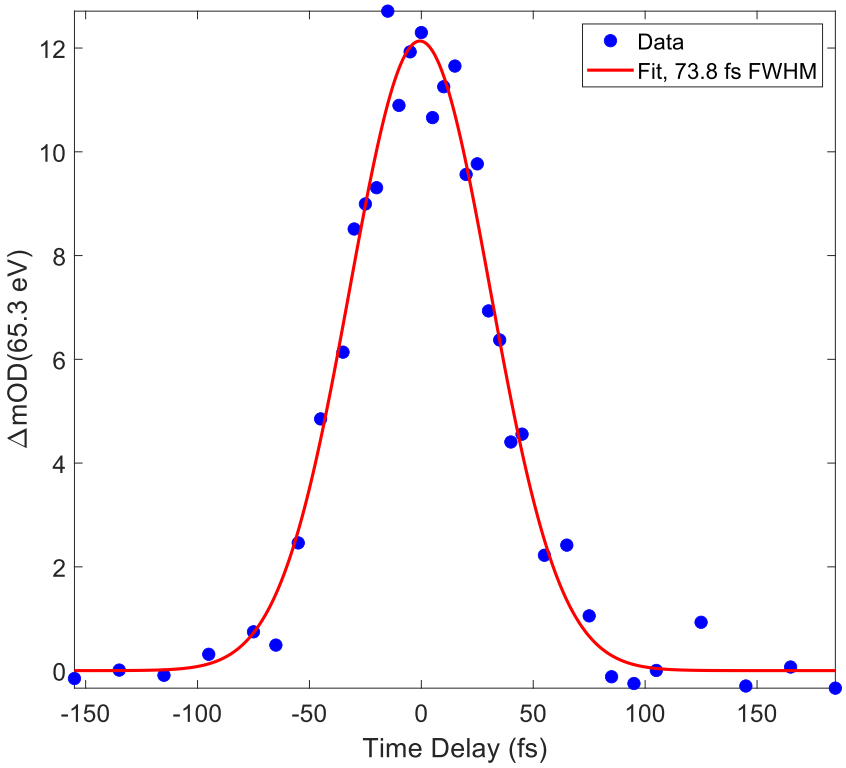

Figure S8: Cross correlation measurement between the 266 nm and XUV pulses via ponderomotive shifting of the $^2D_{5/2} \rightarrow {}^2P_{3/2}$ transition in Xe.

S8 Additional Theoretical Data

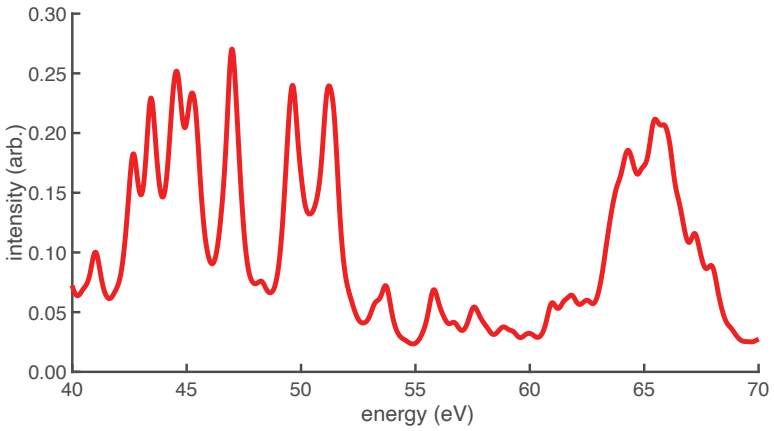

Figure S9: Spin-orbit inclusive TDDFT calculation of the $N_{4,5}$-edge spectrum of AcI using ωB97X-D3. The aug-cc-pVTZ-DK basis set was used for C, H, and O atoms with aug-cc-pwCVTZ-DK3 for I. Although this is consistent with our treatment of valence excitations with TDDFT, the accuracy seems questionable due to spurious large bands appearing at < 50 eV and > 60 eV that do not appear in CVS-EOM-CCSD calculations.

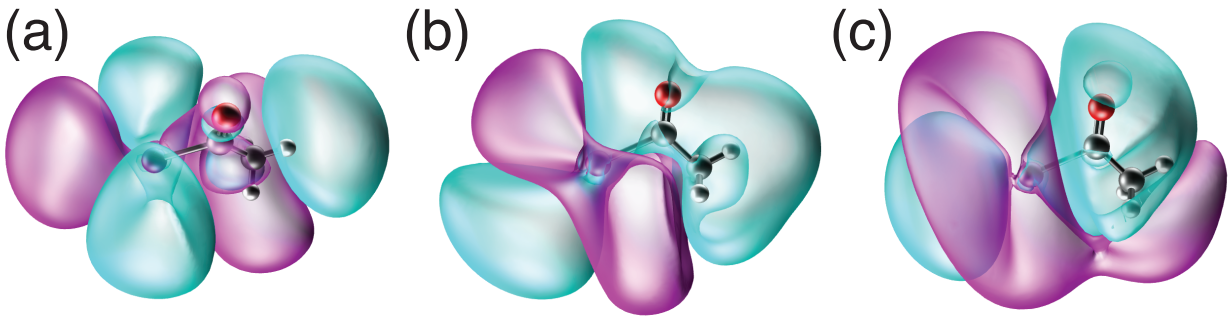

Figure S10: Examples of the I $5d$ orbitals that comprise the acceptor space for the two highest-energy doublet features in the static AcI absorption spectrum as predicted by CCSD. The orbitals that contribute to these excitations are the (a) $5d_{xy}$ or $5d_{x^2-y^2}$, (b) $5d_{xz}$ or $5d_{yz}$ and (c) $5d_{z^2}$. As can be seen, they are all strongly hybridized with the C_2H_3O orbitals.

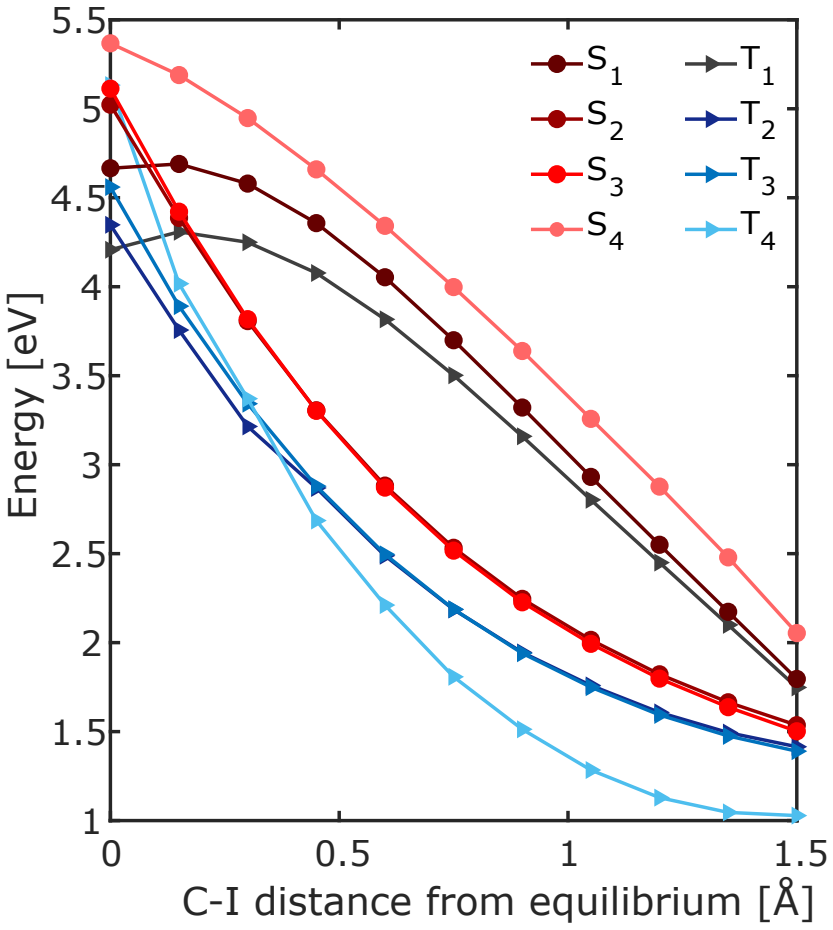

Figure S11: TDDFT potential energy surfaces along the C–I dissociation coordinate of acetyl iodide computed at the ωB97X-D/Def2-ma-TZVPP level. Ground-state geometries were optimized at each step.

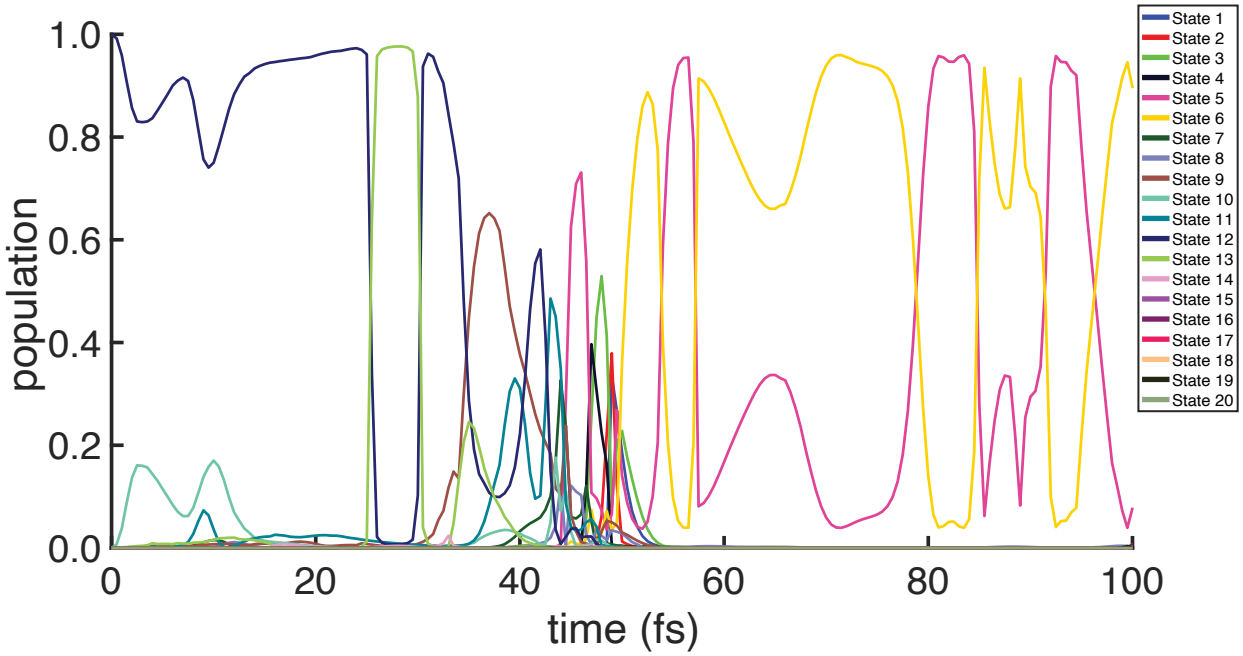

Figure S12: Populations for each state across the TDDFT nonadiabatic molecular dynamics trajectory. These states include 5 spin-pure singlets and 5 triplets, each with M_s=-1, M_s=0, and M_s=+1 components for a total of 20 states.

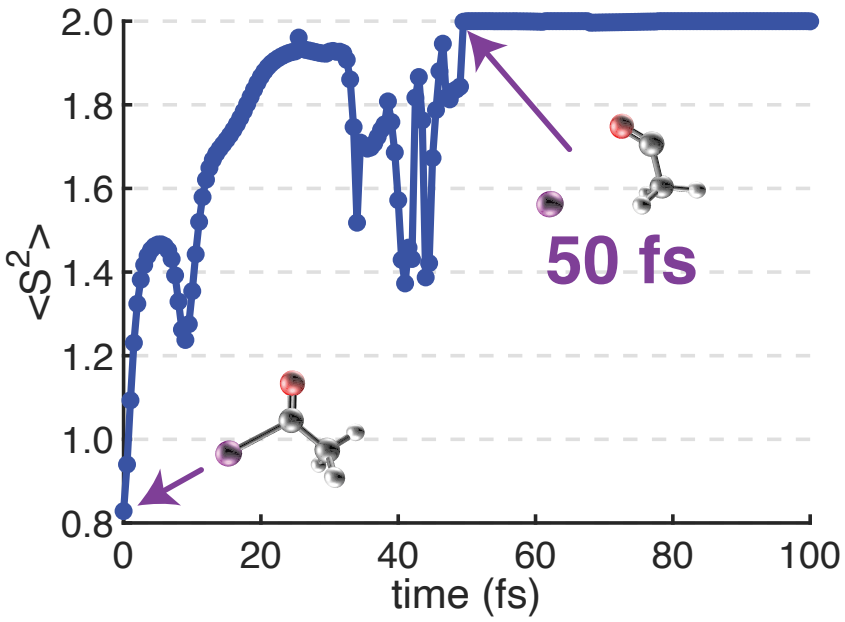

Figure S13: $\langle \hat{S}^2 \rangle$ at each snapshot along a 100 fs *ab initio* molecular dynamics trajectory. The point at which homolytic bond cleavage is achieved is roughly the point at which $\langle \hat{S}^2 \rangle = 2$, which we observe at precisely 50 fs. The inset structures show the geometries at t_0 and $t = 50$ fs.

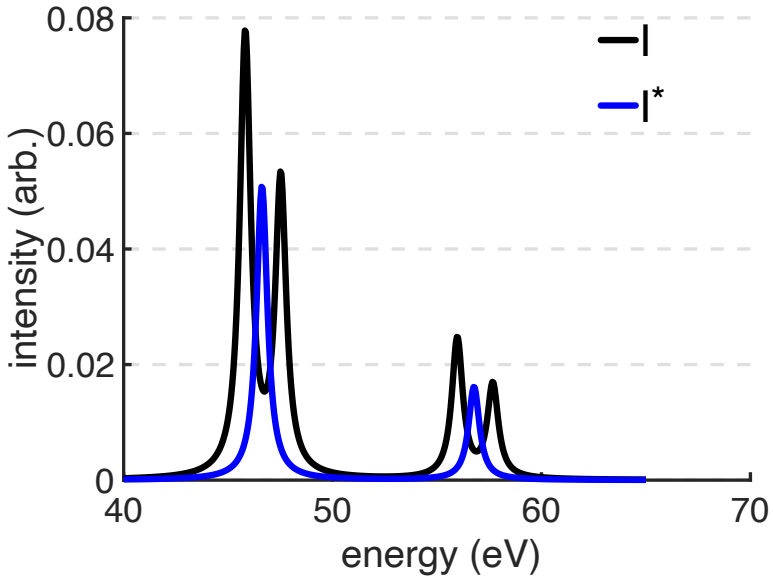

Figure S14: Static absorption spectrum of I ($^2P_{3/2}$) and I* ($^2P_{1/2}$) as predicted by CCSD with atomic spin-orbit corrections.

References

[1] Keller-Rudek, H.; Moortgat, G. K.; Sander, R.; Sörensen, R. The mpi-mainz uv/vis spectral atlas of gaseous molecules of atmospheric interest. *Earth System Science Data* **2013,** *5,* 365–373.

[2] Khamaganov, V.; Karunanandan, R.; Rodriguez, A.; Crowley, J. N. Photolysis of CH3C(O)CH3 (248 nm, 266 nm), CH3C(O)C2H5 (248 nm) and CH3C(O)Br (248 nm): pressure dependent quantum yields of CH3 formation. *Phys. Chem. Chem. Phys.* **2007,** *9,* 4098-4113.

[3] Neese, F.; Wennmohs, F.; Becker, U.; Riplinger, C. The ORCA quantum chemistry program package. *J. Chem. Phys.* **2020,** *152,* 224108:1–18.

[4] Lin, Y.-S.; Li, G.-D.; Mao, S.-P.; Chai, J.-D. Long-range corrected hybrid density functionals with improved dispersion corrections. *J. Chem. Theory Comput.* **2013,** *9,* 263–272.

[5] Dunning, Jr., T. H. Gaussian basis sets for use in correlated molecular calculations. I. The atoms boron through neon and hydrogen. *J. Chem. Phys.* **1989,** *90,* 1007–1023.

[6] Kendall, R. A.; Dunning, Jr., T. H.; Harrison, R. J. Electron affinities of the first-row atoms revisited. Systematic basis sets and wave functions. *J. Chem. Phys.* **1992,** *96,* 6796–6806.

[7] de Jong, W. A.; Harrison, R. J.; Dixon, D. A. Parallel Douglas-Kroll energy and gradients in NWChem: Estimating scalar relativistic effects using Douglas-Kroll contracted basis sets. *J. Chem. Phys.* **2001,** *114,* 48–53.

[8] Helmich-Paris, B.; de Souza, B.; Neese, F.; Izsák, R. An improved chain of spheres for exchange algorithm. *J. Chem. Phys.* **2021,** *155,* 104109:1–14.

[9] Douglas, M.; Kroll, N. M. Quantum electrodynamical corrections to the fine structure of helium. *Ann. Phys.* **1974,** *82,* 89–155.

[10] Hess, B. A. Applicability of the no-pair equation with free-particle projection operators to atomic and molecular structure calculations. *Phys. Rev. A* **1985,** *32,* 756–763.

[11] Hess, B. A. Relativistic electronic-structure calculations employing a two-component no-pair formalism with external-field projection operators. *Phys. Rev. A* **1986,** *33,* 3742–3748.

[12] de Souza, B.; Farias, G.; Neese, F.; Izsák, R. Predicting phosphorescence rates of light organic molecules using time-dependent density functional theory and the path integral approach to dynamics. *J. Chem. Theory Comput.* **2019,** *15,* 1896–1904.